Nanoscale Horizons

ROYAL SOCIETY OF CHEMISTRY

COMMUNICATION

View Article Online
View Journal

Cite this: DOI: 10.1039/d5nh00572h

Received 11th August 2025,
Accepted 13th January 2026

DOI: 10.1039/d5nh00572h

rsc.li/nanoscale-horizons

Ambient microdroplet synthesis of Pt and Pt–Cu nanorods from homogeneous solutions for electrocatalytic nitrate reduction

Kandampully Sahadevan Aswathi,[a] Keerthana Unni,[a] Sinchan Mukhopadhyay,[a] Anirban Som,[a] Soham Chowdhury,[a] Sourav Kanti Jana,[a] Depanjan Sarkar*[ab] and Thalappil Pradeep*[ab]

In this article, we report a rapid, ambient microdroplet-driven synthesis that directly converts homogeneous solutions of metal precursors into bimetallic nanorods within minutes. Using platinum(II) acetylacetonate as a model precursor, we demonstrate the one-step, reductant-free formation of platinum nanorods. Furthermore, this strategy is extended to mixed solutions of platinum(II) acetylacetonate and copper(II) acetate, enabling the first-time synthesis of platinum–copper bimetallic nanorods *via* ambient microdroplets from simple salt precursors. This facile synthesis proceeds without additional chemical reducing agents and affords nearly quantitative conversion, highlighting the sustainability and efficiency of ambient microdroplet chemistry for creating anisotropic, high-surface-area nanostructures. The resulting platinum and platinum–copper nanorods feature unique bimetallic junctions and enhanced surface area-to-volume characteristics. When evaluated for electrocatalytic nitrate reduction, these nanorods exhibit efficient ammonia production, underscoring the potential of this rapid and sustainable synthetic approach for environmentally relevant catalytic applications. While these results establish a promising platform for environmentally relevant catalysis, further optimization of catalyst composition is required to realize practical applications.

New concepts

This work demonstrates, for the first time, a rapid, ambient microdroplet-driven synthesis that directly transforms simple metal salt precursors into anisotropic monometallic and bimetallic nanorods (NRs) without chemical reducing agents, templates, or harsh conditions. The method enables precise integration of bimetallic junctions and high surface area-to-volume architectures, not readily accessible through conventional electrodeposition or solvothermal synthesis. By exploiting the unique interfacial and confinement effects in microdroplets, we achieve one-step, reductant-free formation of Pt and Pt–Cu NRs within minutes, with nearly quantitative conversion. What distinguishes this approach is its sustainability, operational simplicity, and scalability under ambient conditions, while providing enhanced control over anisotropy and composition. Mechanistically, the work reveals how the reactive microdroplet environment promotes rapid nucleation and directional growth, bypassing the need for external reductants. Functionally, the resulting Pt–Cu NRs display superior electrocatalytic performance for nitrate reduction to ammonia, including improved onset potential and nearly doubled yield compared to Pt-only nanorods, attributed to synergistic effects between Pt and Cu. This concept not only introduces a greener pathway for fabricating advanced nanostructures but also offers new design principles for developing sustainable catalysts for environmental remediation and nitrogen management.

Introduction

In recent years, ambient-charged microdroplets have gathered significant attention from the scientific community due to their intriguing ability to enhance reaction rates and facilitate the creation of new materials.[1–10] Ambient microdroplets offer versatile application platforms representing a remarkable convergence of science and engineering. Unlike synthesis in controlled environments, ambient microdroplets exploit the dynamic environment of confined liquids in open-air settings. Our research group has demonstrated that ambient microdroplets can effectively synthesize functional nanomaterials with a wide range of dimensionalities, from 0D to 3D.[8,11–17] By manipulating deposition conditions, we have successfully created nanostructured materials for diverse applications like catalysis, atmospheric water capture, water disinfection applications, *etc.*[8,15,18] Among the most promising directions for future research is the ambient microdroplet-mediated synthesis of bimetallic nanostructures, particularly those composed of catalytically active metals such as platinum (Pt) and copper (Cu). These bimetallic nanomaterials often display enhanced activity and selectivity due to synergistic effects at their interfaces, making them attractive for both oxidation and reduction reactions in various catalytic processes.[19–28] Recent studies have unveiled that controlling the morphology of Pt-based

[a] *DST Unit of Nanoscience (DST UNS) and Thematic Unit of Excellence (TUE), Department of Chemistry, Indian Institute of Technology Madras, Chennai – 600036, India. E-mail: depanjan_coe@icsrpis.iitm.ac.in, pradeep@iitm.ac.in*
[b] *Centre of Excellence on Molecular Materials and Functions, Department of Chemistry, Indian Institute of Technology Madras, Chennai – 600036, India*

nanomaterials can significantly enhance their catalytic performance, especially for environmentally relevant reactions such as nitrate reduction. This has led to rapid advances in electrocatalytic nitrate conversion techniques, with several Pt and bimetallic systems showing remarkable activity and selectivity.[29,30]

Microdroplets, which are micro-sized reactors, offer a powerful route to directly assemble alloy nanostructures with controlled size, composition, and morphology, all in a rapid, reagent-free manner. Yet, direct microdroplet-driven synthesis of anisotropic bimetallic nanorods (NRs) from simple salt solutions, especially under ambient conditions and without external reducing agents, has not been reported. Developing such a facile, rapid, and sustainable synthetic approach remains a critical challenge and an important opportunity for the field of nanomaterials.[31,32] Compared with photochemical or electrochemical methods, which leverage external stimuli, such as light irradiation or applied potential, to drive interfacial reactions, promote electron transfer, and enable template-free growth under mild conditions. Ambient microdroplet synthesis utilizes interfacial electric fields to rapidly drive metal ion reduction at the liquid–air interface, eliminating the need for reductants and offering simplicity, sustainability, and compositional control. Its limitations include reduced tunability and sensitivity to droplet size; however, practical scalability sets it apart.

To showcase the practical significance of such advanced microdroplet-synthesized nanostructures, we have chosen to explore their application in a reaction of rising environmental and industrial importance, namely the electrochemical reduction of nitrate (NO_3^-) to ammonia (NH_3). NH_3 is an important feedstock used in fertilizers, chemicals, and fuel.[33–37] Its significance extends further as an advanced energy carrier due to its notable energy density of 4.3 kWh kg^{-1} and environmentally friendly emission profile.[38] However, traditional NH_3 production *via* the Haber–Bosch method necessitates high temperatures and pressures, leading to substantial energy consumption, increased costs, and heightened CO_2 emissions.[39] Hence, developing an alternative, environmentally friendly NH_3 production pathway is imperative, considering global consumption demands.

In this work, we introduce a novel, ambient microdroplet-based synthetic strategy for fabricating anisotropic NRs, with the primary focus on developing a facile and sustainable approach for producing alloy nanostructures. Our method, for the first time, demonstrated the direct formation of bimetallic NRs from simple ionic precursors under ambient conditions, without the need for external reducing agents or harsh chemicals. Specifically, platinum(II) acetylacetonate ($Pt(C_5H_7O_2)_2$) served as a readily available Pt source, which was directly converted to Pt nanoparticles (NPs) of 2–5 nm diameter exclusively *via* ambient charged microdroplets, and the simultaneous deposition of these NPs onto a conductive substrate facilitates their oriented assembly into one-dimensional NRs. By co-introducing copper(II) acetate ($Cu(CH_3COO)_2$) with $Pt(C_5H_7O_2)_2$, we further demonstrated the direct synthesis of Pt–Cu bimetallic NRs, which exhibit a distinctive two-headed, dagger-like morphology. The results reported here are a significant advancement in the sustainable and straightforward synthesis of alloy nanostructures and expand the capabilities of microdroplet chemistry. To illustrate the potential application of these uniquely synthesized nanorods, we conducted proof-of-concept electrochemical experiments, integrating the Pt and Pt–Cu NRs into electrodes and evaluating their performance for the electrocatalytic reduction of NO_3^- to NH_3. Notably, the Pt–Cu bimetallic NRs demonstrated superior catalytic activity compared to their monometallic Pt counterparts. The simplicity and sustainability of the microdroplet-based fabrication process of mono-metallic and bi-metallic anisotropic nanomaterials, and the demonstration of their potential application in nitrate reduction collectively make this approach a valuable advancement for the scalable, environment friendly, and highly controlled synthesis of functional nanomaterials, offering significant promise for both fundamental research and practical applications in catalysis and beyond.

Experimental

Materials

Platinum(II) acetylacetonate (97%), copper(II) acetate monohydrate, platinum black, Nafion™ perfluorinated resin solution (5 wt%), and potassium hydroxide were purchased from Sigma-Aldrich, India. Sodium nitrite, acetone, potassium nitrate, ammonium chloride, and sodium nitrite were purchased from Rankem Chemicals. Carbon fibre paper was bought from Anabond Limited, and glass capillaries used for electrospray fabrication were purchased from Sutter Instrument, USA.

Synthesis of Pt NRs

Pt NRs were synthesized under ambient conditions using a custom-built nanoelectrospray ionization (nESI) source to generate microdroplets from platinum(II) acetylacetonate ($Pt(C_5H_7O_2)_2$) salt precursor. A 5 mM solution of platinum acetylacetonate in acetone was prepared and electrosprayed directly onto water at a potential of 1.6 kV for 20 minutes. The water was electrically grounded by a copper strip connected to the common earth of the laboratory to neutralize the Pt^{2+} ions effectively.

Synthesis of platinum nanorods

Platinum–copper bimetallic nanorods (Pt–Cu NRs) was synthesized by electrospraying an equimolar (5 mM in each case) mixture of $Pt(C_5H_7O_2)_2$ and copper(II) acetate ($Cu(OAc)_2$) onto electrically grounded water for 10 minutes. The deposition time, rate, applied potential, *etc.*, were optimized to get the shape of the desired NRs.

Characterization

Synthesized NRs were characterized using Thermo Scientific Verios G4UC High-Resolution Field Emission Scanning Electron Microscope (HR-FESEM) and High-Resolution Transmission Electron Microscopy (HRTEM) using a JEOL 3010 instrument. High-angle annular dark-field scanning transmission electron

microscopy (HAADF-STEM) was performed using a Thermo Scientific Talos F200X G2 microscope. UV-vis spectroscopic experiments were performed using the PerkinElmer Lambda 365 spectrometer. X-ray photoelectron spectroscopy (XPS) data were measured using an ESCA probe TPD equipped with a polychromatic Mg Kα X-ray source ($h\nu$ = 1253.6 eV). The binding energy of the spectral regions of different elements was calibrated with respect to C 1s (285.0 eV).

Electrochemistry experiments

Electrochemical experiments were performed as described in SI. Briefly this involved preparing an electrode using the NRs and quantifying the reactant (NO_3–) and products (NH_3– and NO_2–).

Results and discussion

Ambient microdroplet-based synthesis

Fig. 1A presents a schematic diagram of the ambient microdroplet-based synthesis setup. A custom-built nanoelectrospray ionization (nESI) source was employed to generate ambient microdroplets. A borosilicate glass capillary with an inner diameter of 0.86 mm and an outer diameter of 1.5 mm was mechanically pulled into two parts using a commercial micropipette puller instrument (purchased from Shutter Instruments, USA), producing tips with an opening of 20–30 μm. Each tip was examined under an optical microscope for quality and size, and those not meeting the specified criteria were discarded. Once a tip met the required standards, it was filled with a 5 mM precursor solution, and a 0.1 mm diameter platinum wire was inserted to establish an electrical connection. Upon applying a high potential, a spray plume was generated, which was directed toward a grounded surface for collection. In this experiment, the grounded surface was water kept in a 2 mL Eppendorf vial that had been cut in half and filled to form a dome-shaped meniscus. Water in the vial was electrically grounded by affixing copper tape to the inner wall of the tube. As the deposition continued, a yellowish-white material appeared floating on the water's surface. This thin film was scooped onto different surfaces for microscopic and spectroscopic analyses.

For FESEM analysis, the sample was scooped using a clean aluminium sheet. Fig. 1B shows an FESEM image of the material synthesized after electrospray-deposition of the $Pt(C_5H_7O_2)_2$ precursor. The deposited sample exhibited rod-like structures with lengths ranging from 500 nm to 1.5 μm (Fig. S1). Following the FESEM imaging, we hypothesized the possibility of deposition of salt crystals. To investigate this, a control experiment was conducted by drop-casting the precursor salt solution onto an aluminium sheet, followed by FESEM imaging. Fig. S2 presents the corresponding FESEM image of the precursor salt crystals. The images clearly demonstrate that the electrospray-deposited samples are distinct from the precursor salt crystals in terms of size, shape, and appearance. While the electrospray-deposited sample appeared as nanorods, the drop-cast samples resembled needle-like crystals. To further examine the resulting NRs, TEM imaging of the as-synthesized material was conducted. This involved electrospraying the $Pt(C_5H_7O_2)_2$ solution onto the water surface for two minutes, which was then scooped with a TEM grid for imaging (Fig. 1C). A control experiment was conducted by directly electrospraying the precursor solution onto a TEM grid. TEM images revealed that the NRs were present (Fig. S3) even with electrospray deposition (ESD) on a solid surface, similar to Fig. 1C. However, the quality of

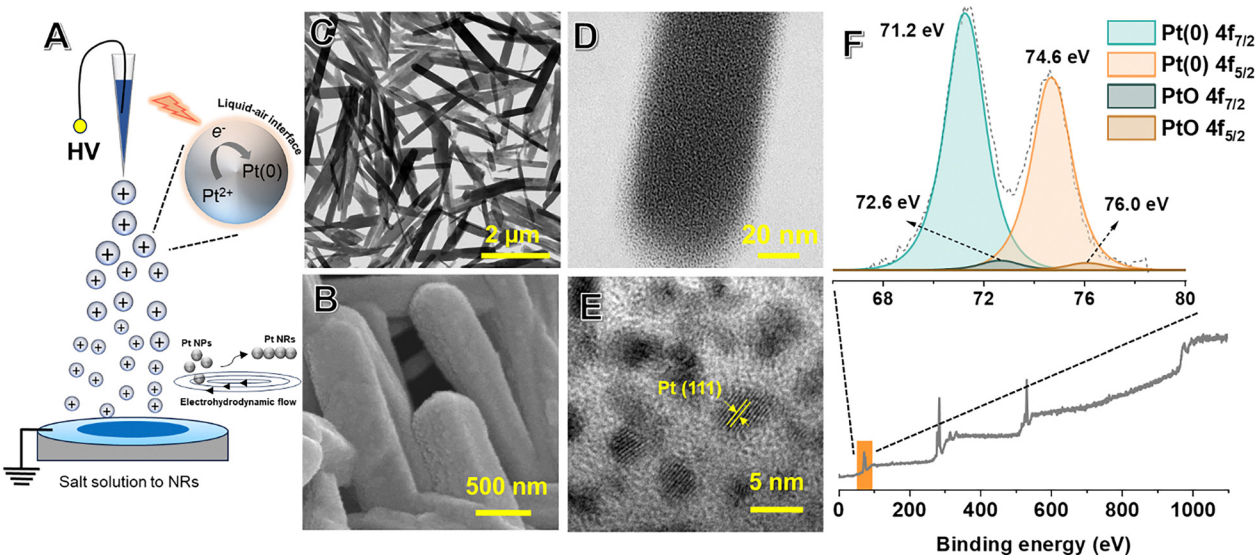

Fig. 1 (A) Schematic diagram of the homemade setup for ambient-charged microdroplet synthesis. Insets demonstrate a schematic representation of the reduction mechanism of the Pt^{2+} precursor, and the electrohydrodynamic motion-induced arrangement of the Pt NPs on the water surface to form the NRs. (B) FESEM image and (C) TEM images of the synthesized Pt NRs, and (D) tip of a single Pt NR at higher magnification, (E) HRTEM image of the same NR showing crystalline Pt NPs as the building block of the resultant NRs. (F) XPS spectrum of Pt NRs, survey spectrum (below), and detailed deconvoluted spectrum of Pt (above).

the synthesized Pt NRs was significantly better in the former case (a detailed discussion of control experiments on various substrates is provided in the following paragraph). Upon further magnification of a single NR, as shown in Fig. 1D, it was revealed that these NRs were composed of tiny Pt NPs, each with a size range of 2–5 nm. Subsequent HRTEM imaging (Fig. 1E) of the NR showed lattice fringes corresponding to the Pt (111) plane. This detailed analysis provided insights into the nanoscale structure and composition of the synthesized NRs. During the electrospray process, Pt^{2+} ions in the charged microdroplets acquire electrons from the grounded surface upon deposition, forming Pt(0). Over time, these Pt atoms coalesce to form NPs. Subsequently, these nanoparticles arrange themselves into NRs, leading to the observed multiple rod-like assemblies. A control experiment was conducted to verify that the Pt NPs were formed during the deposition of the charged microdroplets and not due to high-energy electron beam exposure during imaging. TEM images were captured (Fig. S4) from the same spot before and after 1 minute of electron beam exposure. The absence of any changes confirmed that these nanoparticles were stable under the electron beam and did originate from the ESD process. X-ray photoelectron spectroscopy (XPS) data presented below also confirm the same.

ESD on different substrates

Different substrates, such as activated carbon paper, aluminium sheet, and indium tin oxide (ITO)-coated glass slides, were tested to explore the formation of NRs on various solid surfaces and assess their potential for electrode fabrication. ESD was performed on each substrate for ten minutes, followed by FESEM imaging to evaluate the quality of the synthesized material. Fig. S5A–C displays the corresponding FESEM images for these substrates. In a parallel experiment, Pt NRs were synthesized *via* ESD on water.

FESEM imaging (Fig. S5D) revealed that the NRs synthesized by ESD on water exhibited superior quality in terms of shape and size, compared to those on solid substrates. On solid substrates, the synthesized material tended to form cuboid structures rather than rods. As ESD is known to induce electrohydrodynamic flow in water upon deposition;[12] we speculate that this motion contributes to the uniform formation of the NRs during the ESD process. Hence, ESD on water was chosen to synthesize the Pt NRs for all our subsequent experiments.

Characterization of the Pt NRs

Various spectroscopic techniques were employed to characterize the Pt NRs further. Energy dispersive spectroscopy (EDS) indicated that these NRs predominantly comprise Pt (Fig. S6). The carbon and oxygen features observed in the EDS may originate from the substrate (carbon tape in this case), and the unreacted portion of the precursor or residual carbon (the anionic counterpart, acetylacetonate) left behind after the Pt^{2+} ions were neutralized by taking electrons from the electrical ground to form the NPs. UV-vis spectra were measured for the precursor salt solution and the dispersed Pt NRs in acetone after ESD synthesis. As shown in Fig. S7, the UV-vis features of the $Pt(C_5H_7O_2)_2$ solution and the Pt NRs were distinctly different, indicating that the material obtained after ESD is different from the precursor salt. XPS was employed to investigate the valence state of Pt. Fig. 1F presents the XPS analysis of the Pt NRs, showing the survey spectrum and Pt 4f region. The spectrum shows a Pt $4f_{7/2}$ peak at 71.2 eV, supporting a Pt(0) state in Pt NR.[40] A tiny peak at 72.6 eV corresponding to the Pt(II) charge state of platinum oxide was also visible, which may result from the aerial oxidation of the NR surface, as this is an ambient synthesis process.[41] Incomplete reduction of the salt precursor may also be a reason for observing platinum oxide species. Some of the Pt(II) may also arise from the unreacted portion of the precursor.

X-ray diffraction (XRD) analysis was performed on the synthesized Pt NRs. For this experiment, the precursor solution was electrospray-deposited onto an ITO-coated glass substrate for 12 h at a high flow rate (0.1 μL min^{-1}), followed by thin-film XRD measurement. Fig. S8 presents the corresponding XRD spectrum which shows prominent peaks at $2\theta = 39.9^\circ$ and 46.0°, corresponding to the (111) and (200) planes of face-centred cubic (fcc) Pt, respectively. Additional reflections observed below 30° are attributed to unreacted precursor residues (due to the high flow rate of deposition and consequently incomplete conversion), while weak signals associated with Pt oxides are also visible. Several other peaks arise from the underlying ITO-coated glass substrate, which are marked in the figure for clarity.

Growth dynamics of the NRs

After characterization, we tested the feasibility and scalability of the developed synthetic method. Fig. 2 shows an FESEM image of the synthesized Pt NRs over a large area. This demonstrates the possibility of creating substrates coated with NRs. To further understand this process, a detailed investigation was planned to study the growth mechanism of the NRs. A time-dependent ESD was conducted to track the growth dynamics. ESD was performed under identical conditions for two, five, seven, and ten minutes. The resulting materials were imaged using FESEM. Fig. 3A–D shows Pt NRs formed after two, five, seven, and ten minutes of deposition time, respectively. The

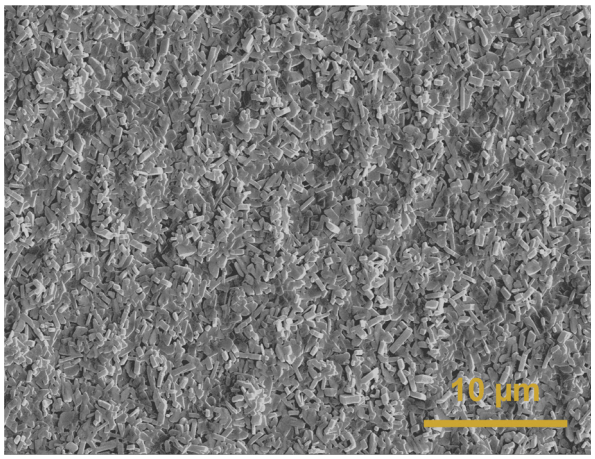

Fig. 2 Large area FESEM image of the Pt NRs synthesized using ambient microdroplets.

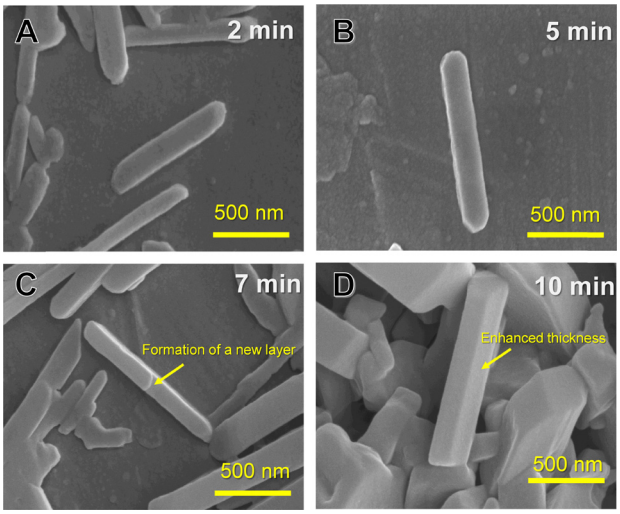

Fig. 3 FESEM images of Pt NRs synthesized with different deposition times: (A) 2 minutes, (B) 5 minutes, (C) 7 minutes, and (D) 10 minutes, illustrating the growth dynamics of the NRs.

FESEM images reveal an increase in thickness over time, suggesting that Pt NPs stack on one another to form the NRs (as indicated in Fig. 3C). Additionally, an interesting observation was made during this experiment: several small bead-like structures were present in the sample made after two minutes of ESD (Fig. S9). These beads were mainly located at the periphery of the circular film formed after two minutes of ESD.

We speculate that these aggregates of nanoparticles were formed because the synthesis process was interrupted midway. This observation supports our earlier hypothesis that the NRs are constructed through the layer-by-layer stacking of nanoparticles, driven by the hydrodynamic flow in water. Typically, the hydrodynamic flow during the electrospray process moves from the center to the periphery of the circular spray spot. This flow pattern likely explains why the nanoparticle aggregates were concentrated at the periphery when the spraying process was stopped prematurely.

Synthesis and characterization of Pt–Cu bimetallic NRs

Recognizing the potential benefits of enhancing catalytic efficiency using bimetallic materials, we further took up the challenge of synthesizing Pt–Cu bimetallic NRs using ambient microdroplets directly from the salt solutions without any external chemicals. Cu was chosen as it is known to enhance both the selectivity and activity of the catalytic process, making it an ideal candidate for improving the performance of Pt-based catalysts. By incorporating Cu into the Pt NRs using the reported microdroplet-based method, we aimed to leverage these synergistic effects to achieve higher catalytic efficiency. Fig. 4 illustrates the Pt–Cu bimetallic NRs synthesized using ambient microdroplets directly from a homogeneous mixture of salt solutions. As detailed in the experimental section, a mixed solution of metal salt precursors was electrosprayed and deposited on various substrates according to the characterization requirements.

FESEM imaging (Fig. 4A) revealed distinct morphological differences between the Pt–Cu bimetallic NRs and the pure Pt NRs. Notably, the addition of copper sharpened the edges

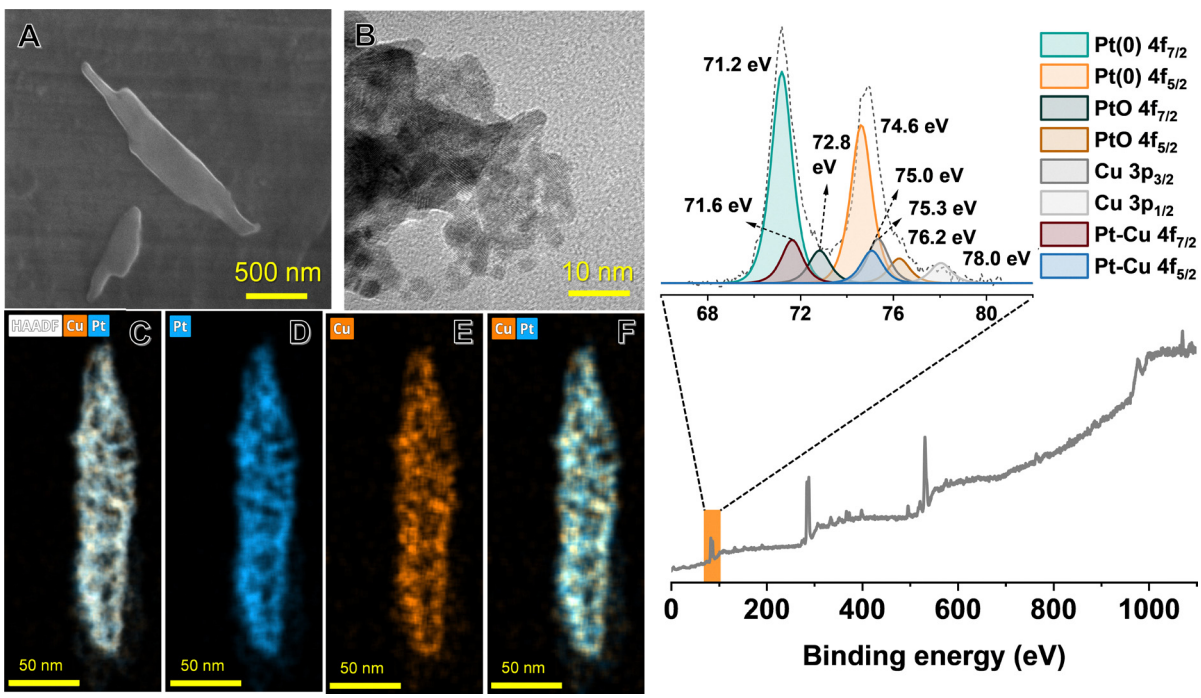

Fig. 4 (A) FESEM image of Pt–Cu bimetallic NR, (B) TEM image of the same demonstrating that these rods are composed of NPs. (C–F) HAADF STEM, along with EDS mapping confirming the uniform distribution of both Pt and Cu in these NRs. (G) XPS analysis of Pt–Cu bimetallic NR, with survey spectrum (below) and detailed deconvoluted spectrum of Pt (above).

of the NRs, giving them a "two-headed dagger" appearance. A large-area STEM image (Fig. S10) clearly highlights (yellow circles) that the Pt–Cu NRs exhibit the characteristic two-headed 'dagger-like' morphology. The EDS spectrum (Fig. S11) collected from one of these NRs further corroborated the presence of both the metals, validating the synthesis process and the formation of the "two-headed dagger" shaped Pt–Cu bimetallic NRs. TEM image captured from the tip of one of these bimetallic NRs (Fig. 4B), confirmed that they were also made of NPs. HRTEM imaging (Fig. 4B) provided a clear view of the lattice fringes of these nanoparticles, indicating their crystalline nature. To further verify the distribution of both Pt and Cu in the NRs, HAADF STEM imaging was performed (Fig. 4C–F). This imaging technique, along with EDS mapping, demonstrated a uniform distribution of Pt and Cu throughout the NRs, confirming the successful formation of bimetallic structures. The EDS spectrum collected from the Pt–Cu NRs, as shown in Fig. 3C–F, indicates the atomic percentages of Cu and Pt to be 6.4% and 93.6%, respectively (Fig. S12). These values are consistent with the SEM-EDS data obtained from a larger area (Fig. S11). Although equimolar Pt(II) and Cu(II) precursors were used, the final NRs are Pt-rich. This apparent compositional asymmetry reflects the higher reduction potential and faster interfacial reduction kinetics of Pt(II) relative to Cu(II) under ambient microdroplet conditions. The preferential nucleation of Pt atoms followed by partial Cu deposition leads to Pt-dominant bimetallic nanorods with limited Cu incorporation, in line with prior observations for Pt–Cu systems synthesized under mild reduction environments.

XPS analysis (Fig. 4G) confirms the incorporation of Cu into the Pt NRs, as evidenced by a peak at 71.6 eV, which is slightly shifted to a higher binding energy compared to the Pt(0) peak at 71.2 eV. This shift can be attributed to the Pt–Cu interaction, consistent with previous observations. Cu 3p peaks overlap within this binding energy range in the deconvoluted spectrum. Additionally, a small amount of platinum oxide (72.8 eV) is detected in the bimetallic NRs, while the majority of platinum remains in the Pt(0) state. Pt and Cu atomic percentages were calculated to be 92.96% and 7.04%, respectively, which again supports the EDS data reported above.

Catalytic property of Pt NRs

To test the catalytic activity of the synthesized Pt NRs, electrochemical NO_3^- reduction, a process that is crucial for environmental remediation and industrial applications, was chosen as a proof of concept. While Pt is typically active for the hydrogen evolution reaction (HER), our study demonstrates that its catalytic properties can be tailored for other reactions, such as nitrate reduction, by using appropriate precursors and optimized synthesis conditions. A homemade H-cell, depicted in Fig. 5A, was used to investigate the electrochemical reduction of NO_3^- to NH_3 using the Pt NRs as the working electrode. Initially, electrodes were fabricated by scooping the as-synthesized Pt NRs from the water using activated carbon paper, which was then protected from damage by drop-casting Nafion™ (a detailed description is provided in the experimental section). The stability

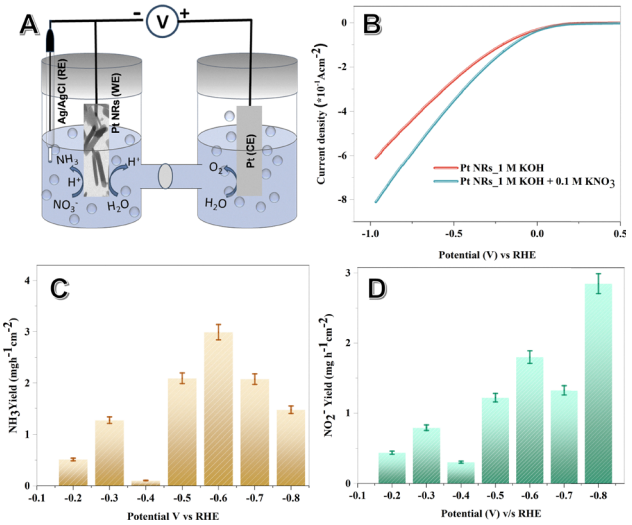

Fig. 5 (A) Schematic representation of the electrochemical H-type cell used for all the electrochemical experiments and the electrochemical reaction process, (B) linear sweep voltametric curves of Pt NRs in the presence and absence of 0.1 M KNO_3, and (C) NH_3 and (D) NO_2^- yields of Pt NRs at different potentials estimated using indophenol method and Griess test, respectively. The *Y*-axis values were divided by a factor of 1000. Error bars represent ±5% experimental uncertainty, illustrating variability across replicate measurements.

of the fabricated electrode was tested by dipping it underwater for 1 h, followed by FESEM imaging. Fig. S13 demonstrates that the electrode was stable under the experimental conditions.

Linear sweep voltammetry (LSV) measurements were conducted both in the presence and absence of NO_3^- (Fig. 5B), revealing a significant increase in cathodic current density when NO_3^- was present. This increase suggests that Pt NRs preferentially reduce NO_3^- over competing H^+ ions, demonstrating their selectivity and effectiveness in NO_3^- reduction. To further understand the catalytic efficiency of the synthesized Pt NRs, their performance was compared with other commonly used substrates, including carbon paper and Pt wire. The LSV results (Fig. S14) indicated that the microdroplet-derived Pt NRs had superior catalytic activity for NO_3^- reduction compared to other candidates. This enhanced performance is attributed to the high surface area of the NRs, which, in turn, was made of Pt NPs and provided more active sites for the catalytic reaction. The higher current density observed for Pt NRs than Pt wire (Fig. S14) reflects their practical advantage in applications where total catalyst loading and surface area are critical design parameters. While intrinsic activity (normalized to electrochemically active surface area) provides mechanistic insight, geometric performance highlights the scalability potential of these nanomaterials. This distinction highlights the importance of selectivity in catalyst design, as Pt NRs demonstrated better selectivity towards NO_3^- reduction. Chronoamperometric measurements were conducted to quantify the products of the electrochemical reduction reaction at various applied potentials over one hour. The primary products were identified as NH_3 and NO_2^-. To accurately determine their yields, the indophenol

method and the Griess test were employed, respectively. The reliability of these measurements depends on achieving precise calibration curves. As shown in Fig. S15, linear calibration curves with an R^2 value of 0.99 were obtained for both the indophenol and Griess tests (a detailed description is provided in the experimental section). The UV-visible spectra of the electrolyte after electrolysis (Fig. S16) showed that the highest NH_3 yield was obtained at −0.6 V *vs.* RHE. The NH_3 yields, displayed in Fig. 5C, demonstrated that the Pt NRs achieved an impressive NH_3 yield of 2989.5 μg h^{-1} cm^{-2} at −0.6 V. We observed a Gaussian pattern of the NH_3 yield with increasing potential (Fig. 5C). The observed trend, where NH_3 yield did not linearly correlate with applied potential, is consistent with the literature,[42] suggesting that HER competes more strongly with NO_3^- reduction at higher potentials, reducing overall efficiency. As mentioned earlier, NO_2^- quantification was also performed using UV-visible spectroscopy, as demonstrated in Fig. S17. Interestingly, while the yield of NH_3 exhibited a non-linear trend with applied potential, the yield of NO_2^- showed a consistent linear increase (Fig. 5D). At −0.4 V *vs.* RHE, the Pt surface becomes saturated with adsorbed H* species, greatly promoting the HER and suppressing nitrate adsorption and reduction. This competition for surface sites lowers the yield of NH_3 and NO_2^-, consistent with literature on potential-dependent surface structure changes in Pt-based electrocatalysts.[43,44] We believe that NO_2^- acts as a key intermediate in the electrochemical reduction of NO_3^- to NH_3. During the reaction, NO_3^- is first reduced to NO_2^-, which then undergoes further reduction to form NH_3. The linear increase in NO_2^- yield with applied potential, as observed in this study, highlights its transient accumulation in the reaction pathway. This intermediate step is influenced by factors such as the applied potential, catalyst properties, and competing reactions like hydrogen evolution to maintain a balance between NO_2^- consumption and NH_3 formation. Understanding this intermediate step and modifying the catalyst accordingly is crucial for optimizing the efficiency and selectivity of the overall reduction process. This prompted us to enhance the efficiency of our catalyst by doping copper into the Pt NRs, as Cu is known for its NO_3^- reduction activity.

NO_3^- to NH_3 conversion using Pt–Cu NRs

Pt–Cu alloys are known to exhibit superior catalytic properties for NO_3^- reduction compared to other bimetallic catalysts involving Pt, primarily due to the synergistic effects between the two metals. The synthesized Pt–Cu bimetallic NRs were tested as catalysts for electrochemical NO_3^- reduction. The electrodes were fabricated and subsequently tested for stability following the same procedure outlined earlier. The LSV results (Fig. 6A) demonstrated a significant decrease in the onset potential (0.02 V *vs.* RHE) in the case of the Pt–Cu NRs as compared to pure Pt NRs, indicating that the addition of copper facilitated feasible NO_3^- reduction, and there was a notable change in the onset potential and current density for the Pt–Cu NRs when comparing the LSV results conducted with and without the presence of KNO_3 (Fig. S18). In the case of Pt

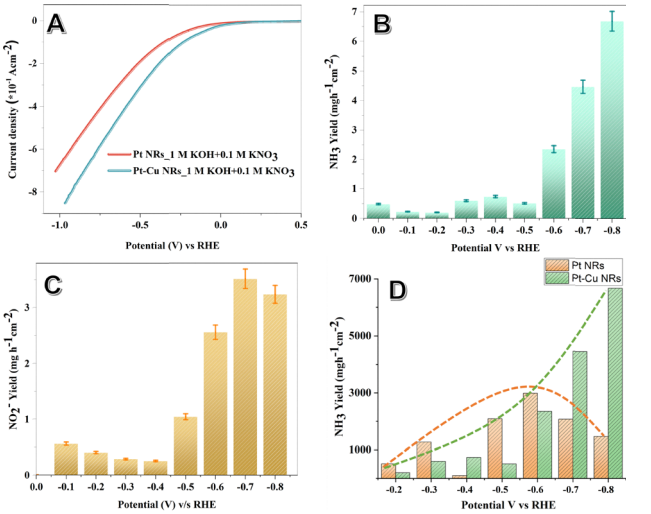

Fig. 6 (A) Linear sweep voltametric curves of Pt and Pt–Cu NRs in the presence of 0.1 M KNO_3 and (B) NH_3, (C) NO_2^- yields for Pt–Cu NRs as the catalyst, at different potentials. The *Y*-axis values were divided by a factor of 1000. (D) Comparison of NH_3 yield between Pt and Pt–Cu NRs across various potentials. The dotted lines show a clear crosspoint at −0.6 V, after which the NH_3 yield decreased in the case of Pt NRs but increased in the case of Pt–Cu NRs.

NRs, the maximum NH_3 yield was achieved at a potential of −0.6 V *versus* RHE (please refer to Fig. 5C). However, for Pt–Cu NRs, the peak yield was observed at a slightly higher potential of −0.8 V *versus* RHE, as evident from the UV-visible spectra presented in Fig. S19 and the bar plot in Fig. 6B. The Pt–Cu bimetallic NRs achieved a remarkable NH_3 yield of 6681 μg h^{-1} cm^{-2} at a potential of −0.8 V, nearly 2.23 times the yield obtained with Pt NRs alone (2989.5 μg h^{-1} cm^{-2}) (Fig. 6B). The NH_3 yield of Pt–Cu NRs was lower compared to Pt NRs at −0.6 V, suggesting that the optimal potential for NO_3^- reduction shifts due to the incorporation of copper. To explore the potential benefits of Pt–Cu NRs, the applied potential was increased to −0.8 V, where the NH_3 yield was found to be 2.23 times higher than that of Pt NRs at their optimal potential. Although HER is a competitive process on Pt-based electrodes, the Pt–Cu NRs demonstrate a marked enhancement in nitrate reduction reaction (NRR) selectivity, as evidenced by the high NH_3 yield and the shift in optimal potential compared to pure Pt NRs. This can be attributed to the synergistic effect at the Pt–Cu interface, where copper promotes NO_3^- adsorption and activation, and platinum facilitates hydrogen transfer for reduction. Similar trends have been reported in recent studies, where bimetallic catalysts exhibit improved NRR performance due to such interfacial effects.[42,45,46] Notably, our NH_3 yield at −0.8 V (6681 μg h^{-1} cm^{-2}) compares favorably with other Pt- and Cu-based catalysts reported in the literature, further supporting the efficacy of our approach. The observed NRR process is likely diffusion-controlled and proceeds through consecutive reduction steps, as is typical for such systems. As indicated by the LSV profiles, the competitive HER underscores the importance of optimizing the catalyst composition and applied potential to maximize NRR selectivity and efficiency. The formation of NO_2^-

as an intermediate was also observed during the electrochemical process for both Pt NRs and Pt–Cu NRs (Fig. 6C). However, a significant distinction was noted: in the case of Pt–Cu NRs, a larger fraction of the intermediate NO_2^- was further converted to NH_3. This is evident from the reduction in NO_2^- concentration at 0.8 V (Fig. S20) and the Gaussian behavior observed, while NH_3 yield showed a consistent linear increase at the same time (Fig. 6D). This is likely due to the dual catalytic roles of the Pt–Cu interface, where copper enhances the adsorption and activation of NO_3^- and NO_2^-, while platinum drives the subsequent reduction steps more effectively. The observed variation in catalytic activity between Pt NRs and Pt–Cu NRs across different potentials can be attributed to their distinct nitrate adsorption and reduction mechanisms. At lower potentials (-0.2 to -0.5 V *vs.* RHE), Pt exhibits higher activity due to its ability to adsorb nitrate in a favorable tridentate configuration on Pt(100) facets, which facilitates the initial NO_3^- to NO_2^- reduction. In contrast, at more negative potentials (> -0.6 V), metallic Cu becomes more active, as its strong NO_3^- adsorption and capability for multi-electron transfer support the complete reduction of nitrate to ammonia. Meanwhile, the competing hydrogen evolution reaction increasingly limits Pt's activity at these potentials. This mechanistic distinction explains the complementary roles and potential-dependent performance of Pt and Cu in nitrate reduction catalysis. Furthermore, the higher applied potential (-0.8 V) in Pt–Cu NRs may provide the additional energy required to overcome activation barriers for converting NO_2^- to NH_3, resulting in a higher overall NH_3 yield. The reduced accumulation of NO_2^- and the preferential conversion of NO_3^- directly to NH_3 further underscore the effectiveness of Pt–Cu NRs in promoting complete reduction pathways. Hence, we could drag the NO_3^- to NH_3 reduction reaction kinetics to the right-hand side by incorporating the Cu into the Pt NRs. Chronoamperometric tests were conducted on the electrodes at their respective optimal potentials, *i.e.*, Pt NRs at -0.6 V and Pt–Cu electrodes at -0.8 V, to assess their stability during the process. Fig. S21 demonstrates that the Pt–Cu NR electrode is equally stable as the Pt NR electrode. Thus, we have highlighted the role of bimetallic interactions in enhancing the catalytic efficiency and selectivity of Pt–Cu NRs for NO_3^- reduction, making them a promising candidate for environmentally significant applications. While faradaic efficiencies were not quantified due to the dominance of HER under the tested conditions, the high ammonia yield demonstrates the practical potential of these catalysts. Further optimization to improve selectivity will be explored in subsequent work.

Conclusions

This study demonstrates a straightforward ambient microdroplet-based synthesis methodology for Pt and Pt–Cu NRs and evaluates the catalytic performance of the materials derived for electrochemical NO_3^- reduction as a model application of the materials. For the first time, we report the fabrication of anisotropic monometallic and bimetallic structures directly from readily available salt precursors using ambient microdroplets, without additional reducing agents, template forming chemicals or harsh conditions. The Pt NRs demonstrated a rod-like structure composed of NPs, confirmed through various imaging techniques, including FESEM, TEM, and HRTEM. The electrospray method enabled the formation of NRs with a high surface area, which is crucial for catalytic applications. Compared to conventional electrode fabrication techniques such as electrodeposition and solvothermal methods, the demonstrated microdroplet-based synthesis offers rapid, ambient-condition fabrication and ensures uniform, high-surface-area Pt–Cu nanorods with well-integrated bimetallic interfaces. This not only enhances catalytic activity and stability but also provides a sustainable and scalable approach for catalyst production. The Pt NRs exhibited good selectivity for NO_3^- reduction, evidenced by a significant increase in current density in presence of NO_3^-, compared to other tested materials, such as activated carbon paper and Pt wire. The synthesized Pt NRs showed an impressive NH_3 yield of 2500 $\mu g\ h^{-1}\ cm^{-2}$ at -0.6 V. The introduction of copper into the Pt NRs to form Pt–Cu bimetallic NRs further enhanced the catalytic performance. The bimetallic NRs showed a decreased onset potential for NO_3^- reduction, attributed to the synergistic effects between copper and platinum. The Pt–Cu NRs achieved a nearly doubled NH_3 yield compared to Pt NRs alone, highlighting the effectiveness of copper in enhancing NO_3^- adsorption and overall catalytic efficiency. Both the Pt and Pt–Cu NR electrodes demonstrated stability under operational conditions, making them promising candidates for sustainable and efficient NO_3^- reduction processes. Overall, this study underscores the potential of using bimetallic nanostructures, particularly Pt–Cu, to improve the efficiency and selectivity of electrochemical NO_3^- reduction. Their stability and performance highlight their potential as sustainable catalysts for mitigating NO_3^- pollution and supporting environmentally significant applications in nitrogen management. Overall, the microdroplet-based fabrication technique not only provides an environmentally friendly and energy-efficient approach to catalyst synthesis but also aligns with the principles of green chemistry, promoting the development of sustainable technologies for environmental remediation. While ambient microdroplet synthesis offers rapid and efficient production of nanomaterials, its scalability presents significant challenges. Achieving complete compositional purity during scale-up is difficult due to the potential retention of unreacted precursors in the final product. Consequently, ongoing efforts aim to optimize reaction parameters to enhance the purity of metal nanomaterials synthesized on a larger scale. For future practical applications, exploring more affordable bimetallic or multimetallic systems may be explored.

Author contributions

KSA.: design of the work, data collection, data analysis, and interpretation, K. U.: FESEM data collection, S. K. J.: helped and supervised the electrochemical measurements., and editing the

article A. S.: TEM measurements, S. C.: XPS data collection and analysis, S. M.: data collection, D. S.: conception and design of work, supervision of data collection and analysis, interpretation of results, drafting and editing of the article. T. P.: supervision of data analysis, interpretation of results, and editing of the final version of the article.

Conflicts of interest

There are no conflicts to declare.

Data availability

The data supporting this article are included in the main article and its electronic supplementary information (SI). No additional data have been deposited in external repositories. Supplementary information: SEM image showing several nanorods with marked length measurements. FESEM image of the $Pt(C_5H_7O_2)_2$ drop-casted on an aluminium sheet. TEM image of Pt NRs. TEM image of a single Pt NR before and after electron beam exposure. FE SEM images of Pt NRs synthesized on different substrate. EDS spectrum of Pt NRs. UV-Vis spectra. XRD spectrum collected from Pt NRs. FE SEM image of the Pt NRs after 2 minutes of ESD. Large area STEM image. EDS spectrum of Pt–Cu NRs collected from a large area. EDS spectrum collected from a single Pt–Cu NR. Stability of the electrode. LSV measurements for different electrode. Calibration curve for quantitation of NH_3 and NO_2^-. UV-visible spectra for NH_3 quantitation experiment using Pt NRs catalysts. UV-visible spectra for NO_2^- quantitation experiment using Pt NRs catalysts. LSV curves with and without the presence of KNO_3. UV-visible spectra for NH_3 quantitation experiment using Pt–Cu NRs catalysts. UV-visible spectra for NO_2^- quantitation experiment using Pt–Cu NRs catalysts. Plots for chronoamperometric measurements. See DOI: https://doi.org/10.1039/d5nh00572h.

Acknowledgements

We acknowledge the ANRF Science and Engineering Research Board (SERB), the Department of Science and Technology (DST), and the Government of India for their research funding. T. P. acknowledges the financial support of SERB SUPRA (SPR/2021/000439). We acknowledge the support of the Centre of Excellence on Molecular Materials and Functions under the institution of Eminence scheme of IIT Madras. K. U. thanks the University Grants Commission (UGC), Government of India, for her fellowship. TEM measurements were performed at the ANRF SERB National Facility for Cryo-Electron Microscopy, IIT Madras.

Notes and references

1 Z. Wei, Y. Li, R. G. Cooks and X. Yan, *Annu. Rev. Phys. Chem.*, 2020, **71**, 31–51.
2 J. K. Lee, S. Banerjee, H. G. Nam and R. N. Zare, *Q. Rev. Biophys.*, 2015, **48**, 437–444.
3 X. Yan, R. M. Bain and R. G. Cooks, *Angew. Chem., Int. Ed.*, 2016, **55**, 12960–12972.
4 J. Ghosh and R. G. Cooks, *TrAC, Trends Anal. Chem.*, 2023, **161**, 117010.
5 J. K. Lee, S. Kim, H. G. Nam and R. N. Zare, *Proc. Natl. Acad. Sci. U. S. A.*, 2015, 201503689.
6 M. F. Ruiz-López and M. T. C. Martins-Costa, *Phys. Chem. Chem. Phys.*, 2022, **24**, 29700–29704.
7 K. Gong, A. Nandy, Z. Song, Q.-S. Li, A. Hassanali, G. Cassone, S. Banerjee and J. Xie, *J. Am. Chem. Soc.*, 2024, **146**, 31585–31596.
8 D. Sarkar, M. K. Mahitha, A. Som, A. Li, M. Wleklinski, R. G. Cooks and T. Pradeep, *Adv. Mater.*, 2016, **28**, 2223–2228.
9 A. Li, Z. Baird, S. Bag, D. Sarkar, A. Prabhath, T. Pradeep and R. G. Cooks, *Angew. Chem., Int. Ed.*, 2014, **53**, 12528–12531.
10 A. Som, D. Sarkar, S. Kanhirathingal and T. Pradeep, *Part. Part. Syst. Charact.*, 2017, **34**, 1700101.
11 A. Ray Chowdhuri, B. K. Spoorthi, B. Mondal, P. Bose, S. Bose and T. Pradeep, *Chem. Sci.*, 2021, **12**, 6370–6377.
12 D. Sarkar, R. Singh, A. Som, C. K. Manju, M. A. Ganayee, R. Adhikari and T. Pradeep, *J. Phys. Chem. C*, 2018, **122**(31), 17777–17783.
13 K. Unni, J. Shantha Kumar, A. Som, D. Sarkar and T. Pradeep, *ACS Sustainable Chem. Eng.*, 2024, **12**, 11957–11967.
14 A. Jana, S. K. Jana, D. Sarkar, T. Ahuja, P. Basuri, B. Mondal, S. Bose, J. Ghosh and T. Pradeep, *J. Mater. Chem. A*, 2019, **7**, 6387–6394.
15 D. Sarkar, B. Mondal, A. Som, S. J. Ravindran, S. K. Jana, C. K. Manju and T. Pradeep, *Glob. Challenges*, 2018, **2**, 1800052.
16 B. K. Spoorthi, K. Debnath, P. Basuri, A. Nagar, U. V. Waghmare and T. Pradeep, *Science*, 2024, **384**, 1012–1017.
17 B. K. Spoorthi, A. R. Chowdhuri, B. Mondal, S. Manna, A. Mahapatra, A. R. Kini and T. Pradeep, *Chem. Commun.*, 2025, **61**, 5577–5580.
18 D. Sarkar, A. Mahapatra, A. Som, R. Kumar, A. Nagar, A. Baidya and T. Pradeep, *Adv. Mater. Interfaces*, 2018, **5**, 1800667.
19 S. Biswas, S. Das and Y. Negishi, *Nanoscale Horiz.*, 2023, **8**, 1509–1522.
20 C. Wang, Y. Shi, D. Qin and Y. Xia, *Nanoscale Horiz.*, 2023, **8**, 1194–1204.
21 A. Ten, C. A. West, S. Jeong, E. R. Hopper, Y. Wang, B. Zhu, Q. M. Ramasse, X. Ye and E. Ringe, *Nanoscale Adv.*, 2023, **5**, 6524–6532.
22 L. Xu, E. Stangland, J. A. Dumesic and M. Mavrikakis, *ACS Sustainable Chem. Eng.*, 2022, **10**, 1509–1523.
23 H. Q. Pham and T. T. Huynh, *ACS Appl. Nano Mater.*, 2021, **4**, 4983–4993.
24 R. Xing, R. Li, L. Tong, B. Li, D. Kong, S. Tian and S. Liu, *J. Nanosci. Nanotechnol.*, 2018, **18**, 8296–8301.
25 C.-M. Zhu, A. Gao, Y. Wang and Y. Liu, *Chem. Commun.*, 2014, **50**, 13889–13892.
26 D. Gao, S. Li, G. Song, P. Zha, C. Li, Q. Wei, Y. Lv and G. Chen, *Nano Res.*, 2018, **11**, 2612–2624.
27 J. Liu, M. Liu, X. Yang, H. Chen, S. F. Liu and J. Yan, *ACS Sustainable Chem. Eng.*, 2020, **8**, 6055–6064.

28 S. Paul, J. F. Koons, M. L. Harrigan, K. Roy and J. E. Dick, *Electroanalysis*, 2025, **37**, e12043.
29 H. Liu, Q.-L. Hong, Y.-C. Yin, F. Shi, P. Chen and Y. Chen, *Energy Mater.*, 2025, **5**, 500068.
30 Z.-H. Yuan, T.-J. Wang, B. Sun, Q.-L. Hong, X. Ai, S.-N. Li, J. Bai and Y. Chen, *Appl. Catal., B*, 2025, **366**, 125041.
31 J. F. Koons, S. Paul and J. E. Dick, *Langmuir*, 2025, **41**, 5524–5533.
32 R. M. C. R. Ramos and M. D. Regulacio, *ACS Omega*, 2021, **6**, 7212–7228.
33 Antonio Zavarce., What is Ammonia? Properties, processes, and applications in Industry, https://inspenet.com/en/articulo/what-is-ammonia-properties-applications/.
34 P. IEA, Ammonia Technology Roadmap, https://www.iea.org/reports/ammonia-technology-roadmap.
35 Thyssenkrupp, Ammonia in agriculture: The engine of plant growth, https://www.thyssenkrupp.com/en/stories/sustainability-and-climate-protection/ammonia-in-agriculture:-the-engine-of-plant-growth.
36 Department of Health, The Facts About Ammonia, https://www.health.ny.gov/environmental/emergency/chemical_terrorism/ammonia_tech.htm?utm_source=chatgpt.com.
37 H. Liu, Y. Jia, X. Huang, Y. Liu, Q. Yang, Z. Chen and J. Xu, *ACS Catal.*, 2025, **15**, 1230–1241.
38 R. Lan and S. Tao, *Front. Energy Res.*, 2014, **2**, DOI: 10.3389/fenrg.2014.00035.
39 A. Valera-Medina, H. Xiao, M. Owen-Jones, W. I. F. David and P. J. Bowen, *Prog. Energy Combust. Sci.*, 2018, **69**, 63–102.
40 A. Singh and K. Miyabayashi, *RSC Adv.*, 2020, **10**, 362–366.
41 X. Du, S. Luo, H. Du, M. Tang, X. Huang and P. K. Shen, *J. Mater. Chem. A*, 2016, **4**, 1579–1585.
42 K. Zhang, Y. Liu, Z. Pan, Q. Xia, X. Huo, O. C. Esan, X. Zhang and L. An, *EES Catal.*, 2024, **2**, 727–752.
43 I. M. Tidswell, N. M. Markovic and P. N. Ross, *J. Electroanal. Chem.*, 1994, **376**, 119–126.
44 G. Zhong, T. Cheng, A. H. Shah, C. Wan, Z. Huang, S. Wang, T. Leng, Y. Huang, W. A. Goddard and X. Duan, *Proc. Natl. Acad. Sci. U. S. A.*, 2022, **119**, e2208187119.
45 D. K. K. Kori and A. K. Das, *ACS Appl. Eng. Mater.*, 2023, **1**, 2386–2396.
46 Q. Ding, W. Zhang, Y. Zhu, L. Wang, X. Feng, Y. Xi and X. Lin, *RSC Adv.*, 2021, **11**, 34355–34368.

